



An enhanced phenomenological model to predict surface-based localised corrosion of magnesium alloys for medical use

Title	An enhanced phenomenological model to predict surface-based localised corrosion of magnesium alloys for medical use
Author(s)	Quinn, Conall;Van Gaalen, Kerstin;McHugh, Peter E.;Kopp, Alexander;Vaughan, Ted J.
Publication Date	2023-01-05
Publisher	Elsevier
Repository DOI	10.1016/j.jmbbm.2022.105637

**An Enhanced Phenomenological Model to predict Surface-based Localised Corrosion of
Magnesium Alloys for Medical Use**

Conall Quinn¹, Kerstin Van Gaalen^{1,2}, Peter E. McHugh¹, Alexander Kopp², Ted J. Vaughan^{1*}

¹Biomedical Engineering and Biomechanics Research Centre, School of Engineering, College of
Science and Engineering, University of Galway, Galway, Ireland; ted.vaughan@nuigalway.ie

²Meotec GmbH, 52068 Aachen, Germany; alexander.kopp@meotec.eu

** Corresponding Author*

Dr. Ted J Vaughan

Biomechanics Research Centre (BioMEC)

School of Engineering,

College of Science and Engineering,

University of Galway,

Galway,

Ireland

Phone: (353) 91-493084

Email: ted.vaughan@nuigalway.ie

ORCID: 0000-0002-2219-7620

Keywords

Magnesium; WE43MgO; Corrosion; Degradation; Finite Element; Degradable Metal; Implant

Abstract

This study developed an enhanced phenomenological model for the predictions of surface-based localised corrosion of magnesium alloys for use in medical applications. The modelling framework extended previous surface-based approaches by considering the role of β -phase components throughout the material volume to better predict spatial and temporal aspects of surface-based corrosion in magnesium alloys. This enhanced surface-based corrosion model offers many advantages as it (i) captures multi-directional pitting, (ii) captures various pit morphologies, (iii) eliminates mesh sizing effects, (iv) reduces computational cost through custom time controls (v) offers control of pit sizing and (vi) produces corrosion rates that are independent of pitting parameter values. The model was fully implemented in three dimensions within the finite element framework and shows excellent potential to enable robust predictions of the long-term performance of magnesium-based implants undergoing corrosion.

1. Introduction

Magnesium alloys show promising potential in both orthopaedic and cardiovascular implant applications as they avoid long-term complications associated with permanent metallic implants. Several materials used in permanent metallic implants suffer from the release of toxic metallic ions through wear or corrosion [1-4], which results in inflammatory cascades and tissue loss [5, 6]. Magnesium on the other hand is biodegradable such that its by-products are metabolized by the body [7] and play an important role in all living organisms' dietary systems [8]. However, magnesium-based implants present certain challenges as its high corrosion rate in a physiological environment [9-12] can lead to rapid deterioration of mechanical properties, leading to implant failure before tissue repair has completed [12, 13].

Magnesium is the least noble material of the galvanic series with a standard electronic potential of -2.37V [14], making it highly susceptible to galvanic corrosion. Magnesium along with many other light metals especially when alloyed undergoes non-uniform surface corrosion, therefore understanding and predicting its mechanisms are pivotal to developing implantable magnesium devices. Galvanic corrosion usually occurs due to the presence of impurities or the accumulation of secondary cathodic phases in the microstructure. This generally occurs when the metal contacts a more noble material inside a conductive medium, which leads to localised corrosion around the contact area. Since magnesium is the least noble metal, it is always consumed by anodizing, whereby electrons migrate from the magnesium alpha (α) phase to different cathodes releasing magnesium ions (anodic reaction). These magnesium ions either diffuse to the surface to form corrosion products or are dissolved in the surrounding aqueous environment [15]. Internal galvanic corrosion is due to the existence of grains of impurities and alloying elements at the grain boundaries, schematically represented in Figure 1A. External galvanic corrosion occurs due to contact with a nobler metal as shown in Figure 1B. The α grains consist of either pure magnesium, or a solid solution of magnesium and alloying elements such as Al, Zn, Ca, Mn, and other rare earth metals [15]. Alloying elements can form secondary particles which facilitate corrosion or enrich corrosion products inhibiting corrosion [16]. Impurities such as Fe, Cu, Ni and Co [17] are the four main elements that significantly influence the corrosion resistance of magnesium [15]. Pitting corrosion is the second most common corrosion type of magnesium and its alloys, defined as localised and random severe corrosion on the surface of the magnesium alloy [15]. Galvanic and pitting corrosion are caused by same underlying electrochemical processes, which are described by Equations (1)-(3), however, they have different initiators and result in different pit morphologies. Pitting corrosion can be characterised as highly localised galvanic corrosion, caused by breakages in the passivation layer exposing the alpha phase to corrosive ions (see Figure 1C). The oxidation layer is in a permanent state of breakdown and repair [18]. Penetration of the oxide layer is generally linked to the heterogeneous inclusion of inter-metallic particles on the oxide film [19]. A breakage in the protective passivation layer exposes the alpha phase to corrosive ions (see Figure 1C).

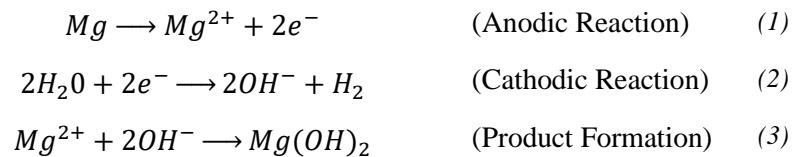
Micro-galvanic cells are created around uncovered secondary areas, resulting in very localised galvanic corrosion and the dissolution of large particles into the surrounding environment. Corrosion continues within the pit until a new passivation layer is precipitated on the surface [14]. Corrosion resistance was found to be significantly less in aqueous environments such as body fluids when compared to atmospheric environment [15] as chloride ions present in the human body transform the corrosive resistant hydroxide layer into soluble magnesium chloride [20]. While corrosion resistance can be increased through protective coatings, alloying [21] and/or mechanical or chemical surface treatments [22], localised pitting corrosion is still an issue for magnesium alloys, which presents distinct challenges for load-bearing implants as the mechanical properties are constantly changing during the lifetime of the device.

Modelling corrosion mechanisms of magnesium alloys has been widely implemented within finite element (FE) frameworks and applied to medical implants to predict in vitro and in vivo performance [23, 24] using either physically based or phenomenological model frameworks. Physically-based models consider the electrochemical interactions and physics of species interaction [5] and these approaches have been applied to magnesium [25] through either activation-controlled [6] or transport-controlled degradation [6]. Activation-controlled models describe the potential difference between the anodic material and the solution. Initially, activation effects were the dominant factor in corrosion, however long-term degradation has been found to be independent of the activation effects [26]. Meanwhile, transport-controlled corrosion models consider the diffusion of magnesium ions from the corroding surface into the corrosive environment. While physically based corrosion models capture the chemical processes taking place, they have mainly been used to model uniform corrosion of the whole implant [27] or localised in small samples to study individual pit growth [27-29]. Physical models are not easily applicable to medical implants due to the difficulty associated with carrying out experimental based calibration for model parameters and the high computational cost associated with modelling electrochemical reactions [8]. The more widely used approach is phenomenological frameworks, which use combinations of a continuum-based damage (CDM) mechanics and/or element removal on the corroding surface to simulate mass loss. These models capture reductions in mechanical strength due to geometrical discontinuities through the definition of a scalar field to quantify the distribution of damage within the model. Many recent corrosion models of this type [8, 24, 27, 28, 30-32], have been based on the approaches proposed by both Gastaldi et al. [8] and Grogan et al. [25], whereby a random distribution function is used to prescribe weighted probabilities across the corroding surface that enable localised pits to form and evolve. While these models can accurately mimic the corrosion rates reported in the experimental literature, they are subject to several limitations. Firstly, very few of these models have been directly compared to experimental samples undergoing corrosion and few, if any, actually capture the severity and spatial distribution of pitting features on the corroding surface [33, 34]. The underlying reason is the geometric simplicity in their approach, whereby corrosion

of the model volume is based only on the parameters prescribed to the initial corrosion surface. This limits how corrosion can evolve and means that models are unable to capture multi-directional or sub-surface pitting, which is a phenomenon that is well-described in experimental literature [32]. Furthermore, these models do not produce any variation in pit morphologies on the corroding surface, with models only producing a characteristic V-shaped pits [25]. Finally, these models tend to a high degree of mesh sensitivity, whereby the initial model discretisation will dictate the overall pit shape/size and, more critically, will actually influence the overall corrosion rate. To better capture localised corrosion mechanisms, more advanced modelling frameworks are required.

In this study, an enhanced phenomenological model for pitting corrosion of magnesium alloys is presented, which extends the original surface-based model that was presented by Grogan et al [25]. This model provides a robust, more effective numerical framework for capturing non-uniform corrosion in metals. The numerical approach implemented using a method that considers corrosion evolution due to the presence of impurities and accumulation of secondary cathodic phases throughout the material (β -phase), that enables the prediction of multi-directional pitting and a range of pit morphologies. The introduction of new parameters to control time incrementation and track excess damage, allows for a reduction in computational cost while retaining model accuracy. The innovative approach development in determining mesh sizing parameter and pitting parameter values allowed for the elimination of mesh sizing effects and provides independence of pitting parameter values and corrosion rate.

Table 1 - Chemical formulation of corrosion process on Mg alloy surface



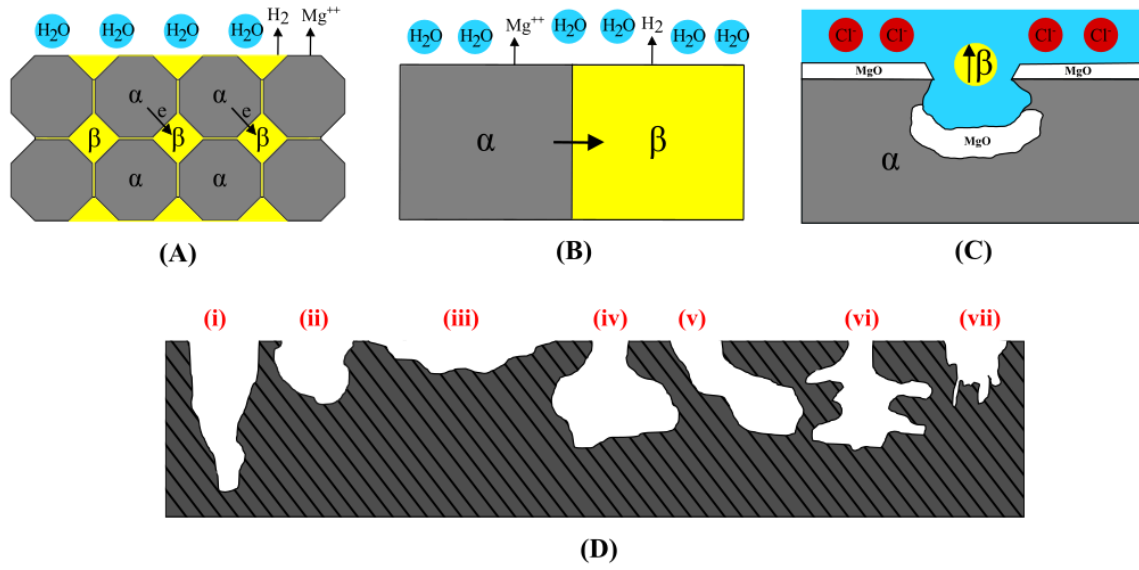


Figure 1- Magnesium alloy/ α phase (grey). Impurities/ β phase (yellow). (A) Internal micro-galvanic corrosion. (B) External galvanic corrosion. (C) Schematic of pitting corrosion. (D) Visual representation of different types of pitting corrosion; (i) Deep & narrow, (ii) elliptical, (iii) wide & shallow, (iv) subsurface, (v) undercutting, (vi) horizontal and (vii) vertical. Image adapted from [35].

2. Methodology

2.1 Surface-based Corrosion Modelling

This study uses a phenomenological approach to pitting, based on continuum damage mechanics theory. The introduction of a scalar damage field (D) ranging from 0 to 1 was used to describe internal geometrical discontinuities (pits, cracks, etc.) representing surface-based corrosion. When $D = 0$ the material element was undamaged, while when $D = 1$, the material element was completely corroded and removed. Continuum damage theory allows non-uniform geometric discontinuities to be modelled, without explicitly capturing volume/mass loss. This was achieved using Equation (4), whereby σ is the true stress and $\bar{\sigma}$ the effective stress,

$$\bar{\sigma} = \frac{\sigma}{1 - D} \quad (4)$$

Surface-based uniform corrosion can be considered through a uniform distribution of micro-galvanic cells, with each element on the corroding surface having the same probability of corroding. This approach describes the corrosion kinetics outlined in Gastaldi et al. [8] and Grogan et al. [25]. Grogan et.al [25] developed the damage evolution law (see Equation (5)) by assigning each element on the corroding surface a random probability, which was capable of modelling non-uniform pitting. Pitting parameter values were only applied to surface elements through the following relation,

$$\frac{dD_e}{dt} = \frac{\delta_U}{L_e} k_u \lambda_e \quad (5)$$

where k_u was the corrosion rate parameter, δ_U and L_e were the material and element characteristic lengths, respectively. By assigning a set of random numbers (λ_e) to the surface elements based on a Weibull distribution function, this model can capture non-uniform corrosion, which is principally governed by the random distribution initially generated on the exposed surface. Following element deletion, the adjacent elements inherited a portion (β) of the removed elements pitting value.

$$\lambda_e = \beta \lambda_{adj} \quad (6)$$

2.2 Enhanced Surface-based Corrosion Framework

The enhanced surface-based corrosion model developed within this study extends the finite element model developed by Grogan et al [25] by considering the role of β -phase components throughout the material volume during the evolution of the corroding surface. Magnesium alloys contain an α -phase (magnesium) and β -phases (alloying metals/impurities) throughout the material volume. The β phase catalyzes the corrosion of the α -phase. The products of the chemical reaction are precipitated onto the cathode protecting it from corrosion. Pitting occurs when the α and β phases are not uniformly distributed, leading to breakdown of the protective layer. The model outlined within this paper phenomenologically captures the different pit morphologies shown in Figure 1D that arise due to microgalvanic corrosion and breakages in the passivation layer cause by aggressive chloride ions [33]. The key difference between our model is that we extend the approach of Grogan et al [25], whereby we prescribe a set of continuous random numbers (λ_{enorm}) to the entire material volume. This enhanced surface-based corrosion model accounts for β -phase components within the material to enable non-uniform and multi-directional evolution of corrosion. Here, we provide an updated damage evolution model that can be described by Equation (7)

$$\frac{dD_e}{dt} = L_{active} k_u \lambda_{enorm} \quad (7)$$

Where L_{active} is an updated term that to accurately account for the characteristic element dimensions. The model workflow is represented schematically in Figure 2, which begins with a pre-processing step (see Section 2.2.1) that defines the model parameters, which ultimately control the rate and shape pitting corrosion within the simulated models. Model parameters can be categorised into two groups: shape parameters (γ (Weibull shape), r_{pit} (Characteristic pit radius) and RS (Random seed)) and rate parameters (k_u (Degradation Rate) and D_{emax} (Time increment control)), described in more detail below. Each element in the finite element mesh is assigned a random number (λ_e), which was used to create a continuous distribution of pitting values (see Section 2.2.2). The algorithm cycles through each element within the model until it finds an exposed magnesium element, resulting in damage accumulation at that location (see Section 2.2.4) determined by an active length parameter (see Section 2.2.3) and local shape and rate parameters. An element removal scheme is implemented, whereby an element is removed

when the critical damage threshold ($D_e \geq 1$) is reached (described in Section 2.2.4). The algorithm cycles through all elements, which enables progressive mass loss on the corroding surface to be captured.

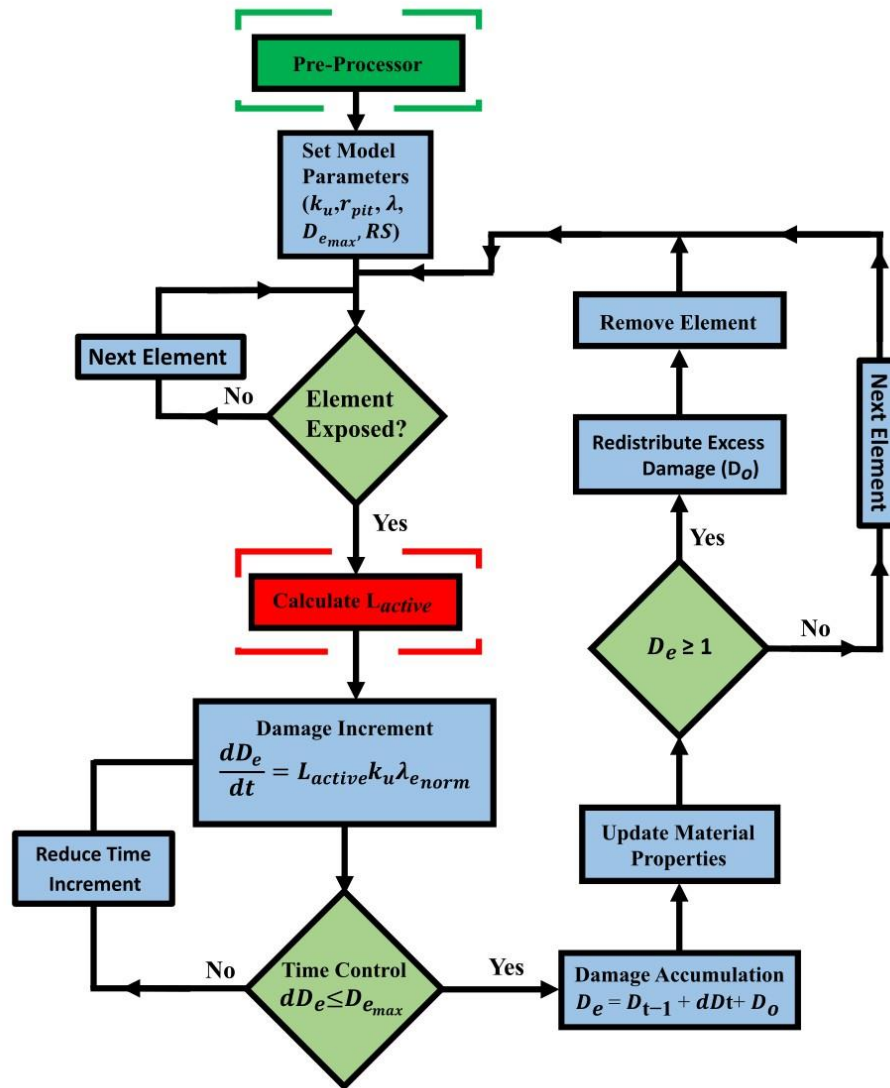


Figure 2 - Overview of enhanced surface-based corrosion damage algorithm.

2.2.1 Pre-Processor

Prior to running a degradation step within Abaqus, a pre-processing step was implemented through Abaqus using python scripting. The pre-processing step extracted model information, initialized model parameters, and generated the random numbers used for corrosion. The pre-processor generated; (A) node labels, nodal coordinates, initial corroding surface, element connectivity and (B) pitting parameter values, as shown in Figure 3.

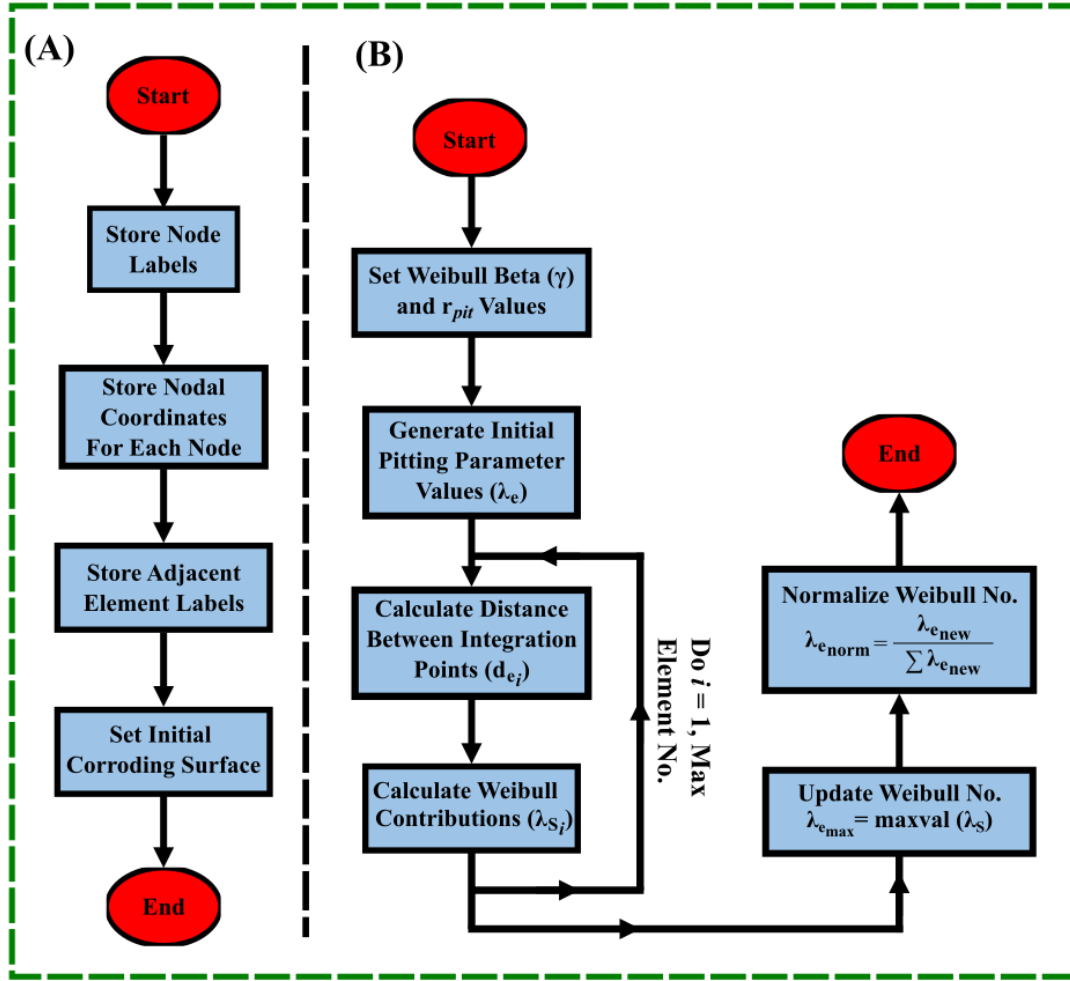


Figure 3 - Basic overview of operations that occur within pre-processor. (A) Stored node labels, nodal coordinates, element connectivity and set initial corroding surface. (B) Calculates the normalised pitting parameter values ($\lambda_{e_{norm}}$).

2.2.2 Pitting Parameter Value Generation

The generation of pitting parameter values occurs within the pre-processor, represented schematically in Figure 3B. The distribution of random pitting parameter values (λ_e) was controlled through the implementation of a Weibull distribution-based random number generator, which used a random seed. The probability of λ_e lying between $[a, b]$ for each element was described by:

$$\Pr[a \leq \lambda_e \leq b] = \int_a^b f(x) dx \quad (8)$$

Where $f(x)$ denotes the standard Weibull distribution probability density function (PDF) described by:

$$f(x) = \gamma(x)^{\gamma-1} e^{-(x)^\gamma} \quad (9)$$

The shape parameter (γ) controls the degree of heterogeneity of the pitting parameter λ_e . Increasing the shape parameter leads to a more uniform distribution, while decreasing the scale parameter leads to more severe pitting, represented schematically in Figure 4D.

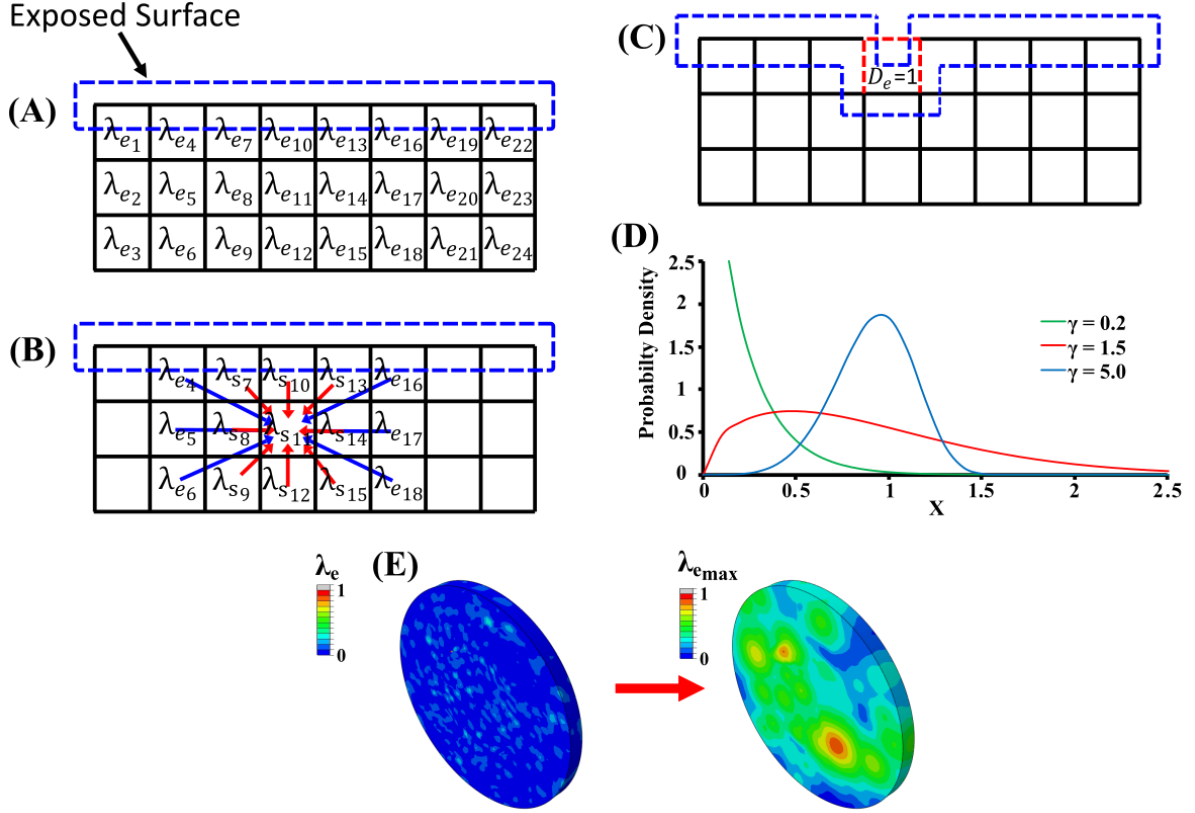


Figure 4 - (A) Pitting parameter values initially assigned to each element within the degrading magnesium sample: (B) Visualization of redistribution of pitting parameters based on Equation (8)(10): (C) Corroding surface updating following element removal: (D) The PDF for a standard Weibull distribution. Decreasing γ leads to a more heterogenous corrosion: (E) Redistribution of pitting parameter values from initial assignment (λ_e) to redistributed pitting parameter values $\lambda_{e_{max}}$.

Based on the generated Weibull distribution, each element within the corroding part was assigned a random number λ_e through an external python script (see Figure 3). This initial assignment of pitting parameter values determined the position and strength of the pit nuclei, from which the pit propagated from Figure 4E. However, by assigning values in this way, a discontinuous spatial distribution of pitting parameters resulted across the mesh. A smoothing step was included to re-distribute the pitting parameters to a continuous distribution across the mesh. For this, a fraction of each element's initial pitting parameter value (λ_{s_i}) was stored based on the distance between its element and other elements within the mesh (d_{e_i}) for all elements in the mesh ($i=1:element\ number$), as represented in Figure 4B. The characteristic pit radius (r_{pit}) was a pre-assigned model parameter that controlled the range of influence of pit nuclei. Individual pits may merge to form a pit larger than r_{pit} .

$$\lambda_{s_i} = \lambda_{e_i} - (\lambda_{e_i})(d_{e_i}) \left(\frac{1}{r_{pit}} \right) \quad (10)$$

The maximum stored pitting parameter value became the active pitting parameter ($\lambda_{e_{max}}$) value (see Equation (11)), where $i=1:element\ number$). This created a continuous distribution of pitting parameter values as shown in Figure 4E.

$$\lambda_{e_{max}} = \max(\lambda_{s_1}, \lambda_{s_2}, \lambda_{s_3}, \lambda_{s_4}, \lambda_{s_5}, \dots, \lambda_{s_i}) \quad (11)$$

In addition, the sum of pitting parameter values within a part can vary dramatically depending on the shape parameter (λ) and characteristic pit radius (r_{pit}) selected. This, in turn, would affect the overall corrosion rate. Therefore, the pitting parameter values were normalised across all elements according to Equation (12), whereby n denotes the number of magnesium elements in the degrading part.

$$\lambda_{e_{norm}} = \frac{\lambda_{e_{max}} n}{\sum_{i=1}^n \lambda_{e_{max}}} \quad (12)$$

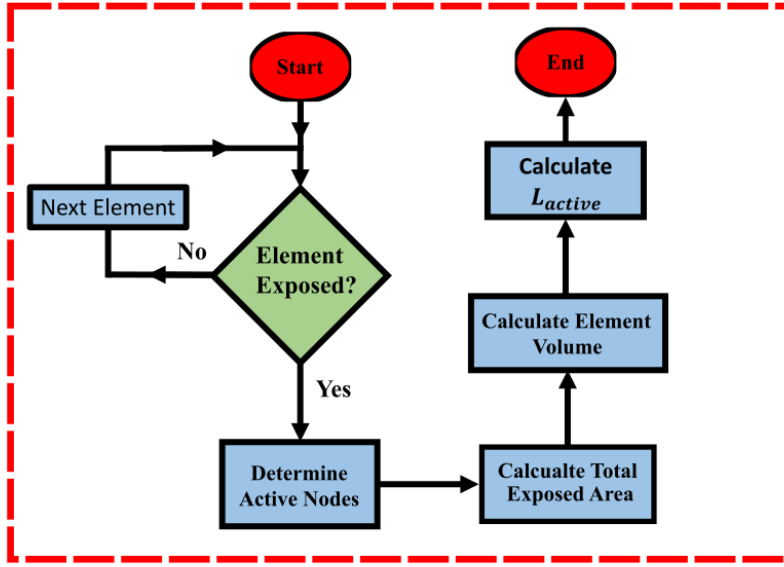
2.2.3 Active Length (L_{active})

Within previous studies [8, 30, 36], the characteristic element length L_e was used to describe the sizing effect of elements within the mesh. The characteristic element length of a brick/quadrilateral element can be described with Equation (13), where V_e and A_e describe the element volume and area respectively,

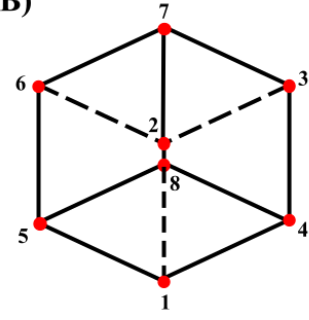
$$L_e = \sqrt[3]{V_e} \quad (13)$$

Gao et al. considered the effect surface area surface area had on corrosion rate [37] by recoding the number of exposed surfaces on each element. However, both these methods assumes that the elements were cubic in shape. When meshing more complex geometries, element shape can vary dramatically, which cannot accurately be described by (13) and results in “mesh effects” that results in sensitivity of the corrosion rate to the discretised geometry. In this model, a sizing parameter was introduced within the framework to geometrically represent the continuous process of corrosion in a discretised manner, while avoiding unwanted sizing effects. A new active length parameter (L_{active}) was introduced at element level to describe the ratio of exposed element surface area to element volume. This required the steps outlined in Figure 5, and below, to calculate the L_{active} parameter.

(A)



(B)



(C)

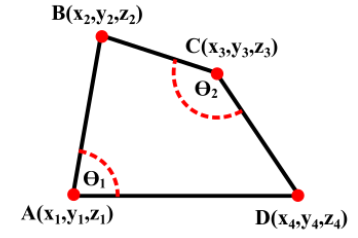


Figure 5 - (A) Processes involved in the calculation of L_{active} on exposed surface. (B) Node connectivity numbering for brick elements within Abaqus. (C) 2-D representation of irregular element face with required variables for calculating element face area.

Node labels and nodal coordinates for each element were extracted within the pre-processing step Figure 3A. The nodal connectivity for brick/quad elements (from Abaqus) is represented schematically in Figure 5B. In terms of node ordering, nodes 1, 2, 3 and 4 will always lie on the same element face Figure 5B. Upon element removal, the shared nodes in adjacent elements were activated. Given all the nodes on element face were active, the surface area was calculated using Equation 14-15. To calculate the area of an irregular quadrilateral, positional vectors from each node A, B, C and D and two opposite angles (θ_1 & θ_2) were required as shown in Figure 5C.

$$\theta_1 = \cos^{-1} \left(\frac{(B - A) \cdot (D - A)}{(|B - A|)(|D - A|)} \right) \quad (14)$$

$$A_{e_{1234}} = 0.5(L_{AB} * L_{AD})\sin(\theta_1) + 0.5(L_{BC} * L_{CD})\sin(\theta_2) \quad (15)$$

The total exposed area ($A_{e_{tot}}$) and active length (L_{active}) was calculated for each element using Equation (16)-(17) respectively.

$$A_{e_{tot}} = A_{e_{1234}} + A_{e_{1256}} + A_{e_{2567}} + A_{e_{3478}} + A_{e_{2367}} + A_{e_{1458}} \quad (16)$$

$$L_{active} = \frac{\sum_{i=1}^6 A_{e_i}}{(L_e)^3} \quad (17)$$

This method allowed for the accurate calculation of element volume, which enabled more robust prediction of corrosion rates in the model.

2.2.4 Damage Evolution, Redistribution and Time Control

The damage increment was calculated using Equation (7). Calculation of the damage increment required the sub-processes outlined in Figure 3 and Figure 5A. Corrosion damage (D_e) was accumulated monotonically by each element on the exposed surface, through the addition of the damage increment (dD_t) to the damage from the previous step (D_{t-1}), as described by Equation (18). The corrosion rate of each element was determined by k_u , $\lambda_{e_{norm}}$ and L_{active} .

$$D_e = D_{t-1} + dD_t + D_o \quad (18)$$

As damage accumulated within an element, the effective mechanical properties were reduced linearly according to Equation (4). When an exposed element becomes completely damaged ($D_e = 1$), the element was removed. Following element removal, any undamaged adjacent element ($D_e = 0$) was activated (Figure 4C).

Within the damage evolution model, a time control was included to control the maximum allowed damage increment ($D_{e_{max}}$) that could occur within a single time increment (see Figure (19)). The algorithm outlined in Figure 2 requires that an element is not fully corroded in a single increment, such that $D_{e_{max}} < 1$. Following the calculation of a damage time step (dt_{new}), the time increment was reduced accordingly.

$$\text{If: } D_e > D_{e_{max}}, dt_{new} = \frac{D_{e_{max}}}{D_e} dt_{old} \quad (19)$$

Damage within an element ranged from undamaged ($D_e = 0$) to completely damaged ($D_e = 1$). Elements on the exposed surface can accumulate damage greater than complete reabsorption $D_e \geq 1$. Excess damage (D_o) was redistributed evenly to adjacent elements ($D_e \leq 1$) on the new/existing exposed surface (see Equation (21)). Where Adj_{el} represented the number of non-absorbed adjacent elements. A sizing term (SR) described the relative size of the current element to its adjacent elements (see Equation (20)). This ensured that when transferring damage from small to large elements or vice versa that the damage was scaled appropriately. Damage redistribution ensured that there was a minimal loss of model accuracy when removing an element and updating the corroding surface

$$SR = \frac{L_{e_{el}}^3}{L_{e_{adj}}^3} \quad (20)$$

$$\text{If: } D_e > 1 \quad D_o = \frac{(D_e - 1)}{Adj_{el}} * SR \quad (21)$$

At the end of a simulated increment, the percentage mass loss was calculated on an element-by-element basis whereby the size of the element was taken into consideration.

$$\% \text{ Mass Loss} = \sum_{i=1}^{\text{Max Elemt No.}} \frac{(L_{ei}^3) * (D_{ei})}{L_{ei}^3} * 100 \quad (22)$$

2.3 Model Verification

Model verification was carried out to investigate the contribution of (i) mesh sizing effects, (ii) mesh density, (iii) Weibull shape parameter (γ) and (iv) time control had on model corrosion. Model geometries and the corroding surface are outlined in Figure 6. The geometry shown in Figure 6A was meshed to two different mesh densities (m_a & m_b) outlined in Table 2. The geometry shown in Figure 6B was meshed to a single mesh density but contained a region of uniformly sized elements (r_a) and a region of irregularly sized elements (r_b). The objectives of each study were outlined below:

- i. To evaluate the effect element size/shape on the corrosion profile.
- ii. To determine the effect mesh density on corrosion rate and model accuracy.
- iii. To determine the effect the Weibull shape parameter λ on corrosion rate.
- iv. To determine the maximum time control ($D_{e_{max}}$) that could accurately predict model corrosion.

Model parameters such as geometry, mesh density, Weibull shape parameter (γ) and time control ($D_{e_{max}}$) are outlined Table 2. Additional model parameters of $k_u = 1$ and $r_{pit} = 5mm$ were kept constant across all simulations. Models were compared to the original surface-based corrosion algorithm, described by Grogan et al. [25] (see Section 2.1) and the newly-developed enhanced surface-based model developed here to provide a direct comparison of model performance.

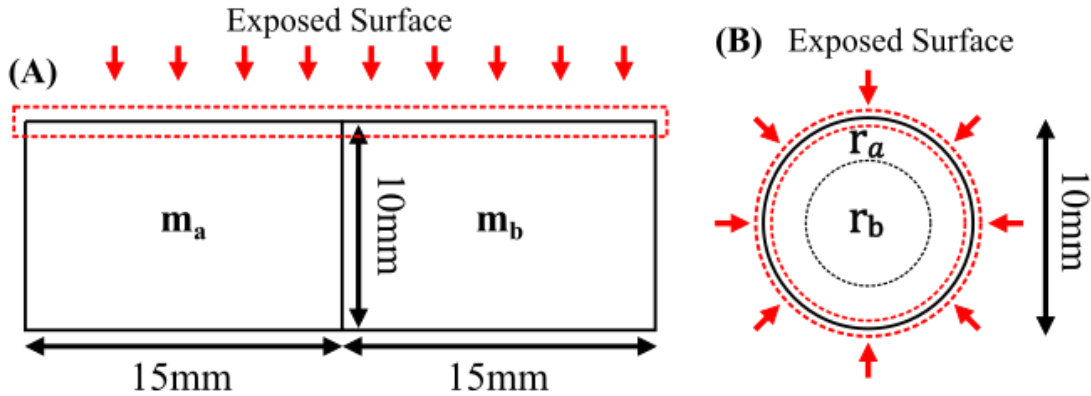


Figure 6 - Model geometries used in model verification study.

Table 2 - Model information used for model verification simulations.

Model No.	Parameter	Geometry	Mesh Density (Elements)	Weibull Shape Parameter (γ)	Time Control ($D_{e_{max}}$)
-----------	-----------	----------	-------------------------	--------------------------------------	--------------------------------

1	Mesh Effect	(A)	$m_a = 15000, m_b = 3800$	Uniform	0.49
2	Mesh Effect	(B)	10,200	Uniform	0.49
3	Mesh Density	(B)	1,632, 2,608, 4,640, 10,200	0.6	0.49
4	Mesh Density	(B)	1,632, 2,608, 4,640, 10,200	Uniform	0.49
5	Weibull Shape Parameter	(B)	10,200	0.2, 0.4, 0.6 & 0.8	0.49
6	Time Control	(B)	10,200	Uniform	0.25, 0.49, 0.75 & 0.99

2.4 Parameter Study

A parameter study was carried out to investigate the effects the Weibull shape parameter (γ), random seed (RS) and characteristic pit radius (r_{pit}) had on the pitting corrosion profile and pit morphology generation. Pitting profiles were captured at 10%, 20%, 30%, 40%, 50%, 60% and 70% mass loss. The model outlined in Figure 7 was modelled as a continuous part with corrosion initiating on the top surface only. While investigating each parameter all other model parameters were kept constant. All simulations were meshed with 5,625 elements and implemented a time increment $D_{e_{max}} = 0.99$. Models 7 and 8 outlined in Table 3 were run with the original surface-based corrosion based on the algorithm outlined by Grogan et al. [25] (see Section 2.1) and the newly-developed enhanced surface-based model developed.

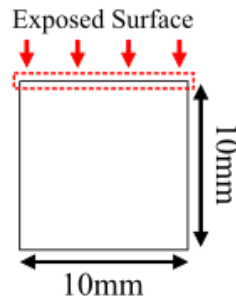


Figure 7 - Model geometry used in parameter study.

Table 3 - Model information used for parameter study simulations.

Model No.	Parameter	Weibull Shape Parameter (γ)	Random Seed (RS)	Characteristic Pit Radius mm (r_{pit})
7	Weibull Shape Parameter	0.2, 0.4, 0.6 & 0.8	2	5
8	Random Seed	0.2	1, 2, 3 & 4	5
9	r_{pit}	0.2	2	2.5, 5, 7.5 & 10

2.5 Three-Dimensional Implementation of Enhanced Surface-based Corrosion Model

The enhanced surface-based corrosion model was implemented to simulate corrosion of WE43MEO (Meotec GmbH, Germany) cylindrical specimens outlined within [33]. The simplified cylindrical geometry outlined in Figure 8 was meshed with 812,120 reduced integration brick elements (C3D8R). Model parameters $\gamma = 0.3$ and $r_{pit} = 0.8$ were implemented to provide the best fit the experimental data. It was assumed that corrosion did not occur on the painted surfaces. Detailed geometrical evaluation of the corrosion models was carried out using an automated detection framework (Pitscan) previously developed [33], and compared to experimental samples undergoing corrosion through micro-CT images [33].

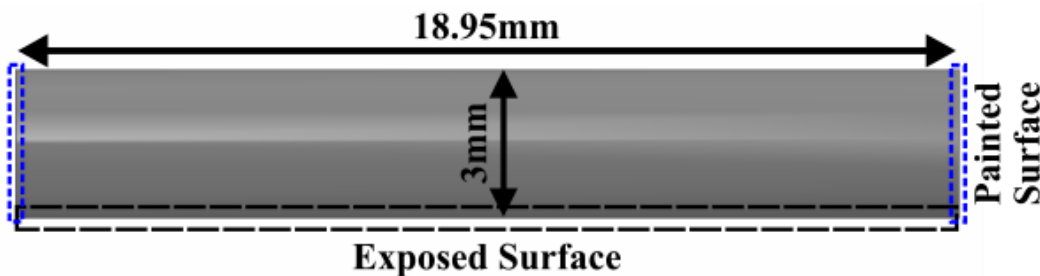


Figure 8 - Simplified dog-bone specimen used to model in-vitro degradation of WE43MEO alloy.

3. Results

3.1 Model Verification

3.1.1 Mesh Sensitivity – Geometric Effects

The effect of mesh sizing on the corrosion response was evaluated by considering a range of corrosion scenarios, outlined in Table 2. Models were degraded using both the original and enhanced surface-based algorithms that implemented L_e and L_{active} as element sizing parameters, respectively. Figure 9 shows the resulting predictions for rectangular sections undergoing uniform corrosion, with two dissimilar mesh densities m_a & m_b . Here, the original surface-based model that uses the sizing parameter L_e is shown to be distinctly sensitive to the different mesh densities across the geometry. Contrastingly, the enhanced model is insensitive to these mesh effects, whereby the correct implementation of L_{active} maintains the original shape across both regions of the part as corrosion progresses (see Figure 9A). Mesh sizing effects are also evident in the original surface-based model when more complex geometries were considered. Considering the circular geometry undergoing uniform corrosion, whereby in the outer region of the circle (r_a) the elements were uniformly sized and in the inner region (r_b) contained varied element sizes. Element removal was largely uniform in the outer region (<75% mass loss), however as the mesh became more irregular (75% - 90% mass loss), substantial mesh effects were evident. On the

other hand, the implementation of the enhanced surface-based corrosion model that uses the L_{active} (see Equation (17) sizing parameter term predicted uniform corrosion regardless of mesh non-uniformity (see Figure 9B)

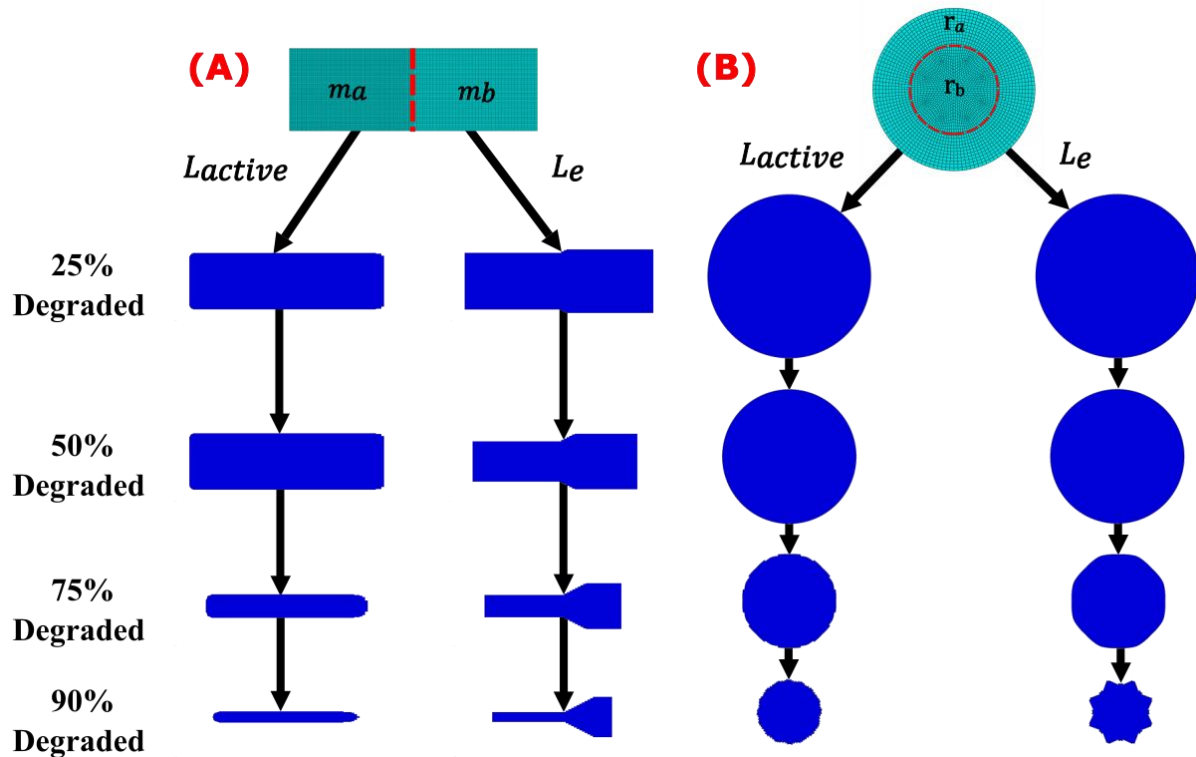


Figure 9 - Visualization of geometric “mesh effects” through the implementation of two sizing parameters L_{active} and L_e . each model was degraded to 25%, 50%, 75% and 90% mass loss. (A) Simple geometry with two different mesh densities (m_a & m_b). (B) Meshing of a complex geometry with a singular mesh density.

3.1.2 Mesh Sensitivity – Rate Effects

The effect of mesh density on corrosion rate was investigated for both original and enhanced surface-based corrosion models. A circular model geometry outlined in Figure 6B was implemented, alongside model parameters for models 3 and 4 described in Table 2. A snapshot of the corrosion profiles for each model at a normalised time (NT) value of 0.5 is shown in Figure 10. Mesh density had little effect on the corrosion rate for both models undergoing uniform corrosion, as shown in Figure 10A. However, for non-uniform corrosion, there was an inverse relationship between mesh density and corrosion rate in the original surface-based model, as shown in Figure 10B, which resulted in distinctly different mass loss % and corrosion profiles at a normalised time of 0.5. On the other hand, the enhanced surface-based corrosion model had a consistent corrosion rate associated with it, converging upon a stable result as the mesh density was increased, as shown in Figure 10B.

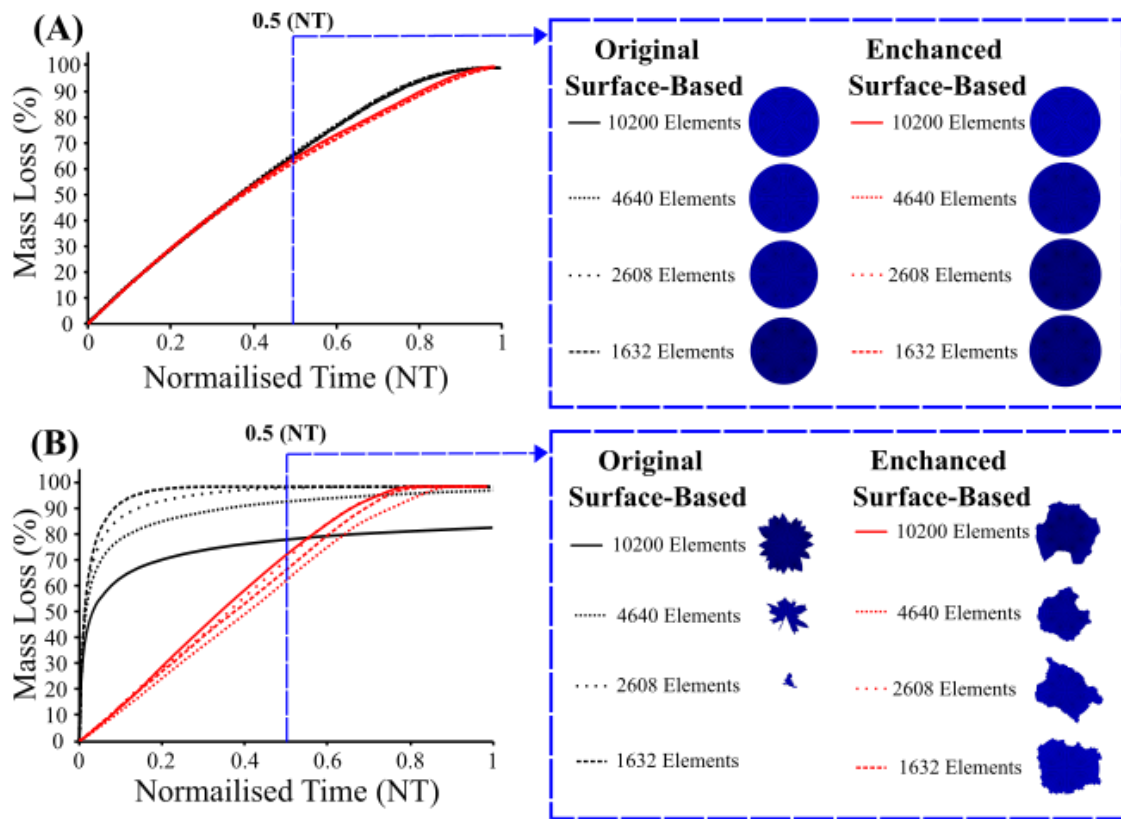


Figure 10 - Percentage mass loss of surface-based (see Section 2.1) and enhanced surface-based corrosion model under (A) uniform and (B) non-uniform corrosion. Degradation profiles were captured for each model was taken at a normalised time (NT) value of 0.5.

3.1.3 Weibull Shape Parameter (γ)

The effect of the Weibull shape parameter (γ) on corrosion rate was investigated for both the original and enhanced surface-based corrosion models. The model geometry outlined in Figure 6B was implemented, alongside model parameters for model 5 described in Table 2. The results show that increasing γ within the original surface-based model decreased the corrosion rate, as shown in Figure 11. Lower γ parameter values resulted in more variance in the distribution of pitting parameter values (see Figure 4D), which in turn resulted in more variation in the degradation rate and substantial differences in the overall corrosion timeframe. Within the enhanced surface-based corrosion model, the corrosion rate remained constant across all values of γ considered (see Figure 11), clearly demonstrating how corrosion rate using this formulation was insensitive to parameter selection

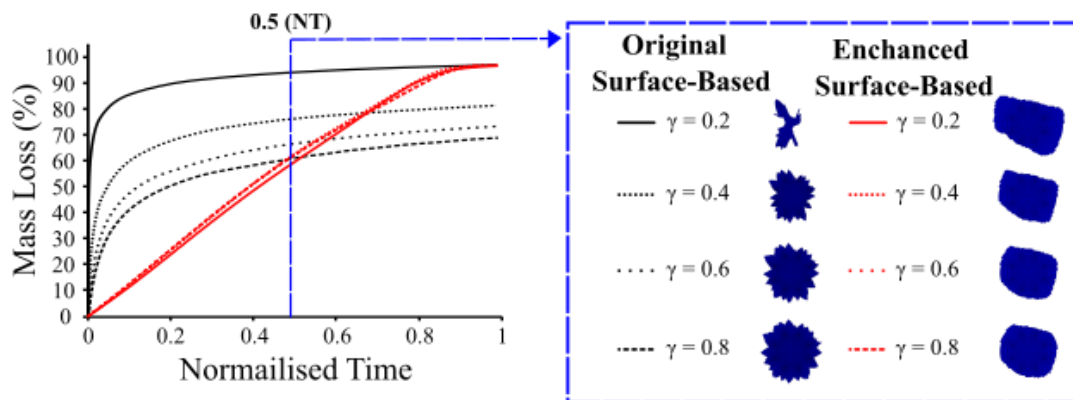


Figure 11 - Percentage mass loss for non-uniform degradation of original surface-based model and enhanced surface-based corrosion model at different Weibull shape parameters. Degradation profiles were captured for each model was taken at a normalised time (NT) value of 0.5.

3.1.4 Time Control ($D_{e_{max}}$)

The effect of the maximum damage per increment ($D_{e_{max}}$) on corrosion rate was investigated for both the original and enhanced surface-based corrosion models. The model geometry outlined in Figure 6B was implemented, alongside model parameters for model 6 described in Table 2. Increasing $D_{e_{max}}$ within the original surface-based model increased the rate of corrosion, as shown in Figure 12. Altering $D_{e_{max}}$ had no effect on the corrosion rate within the enhanced surface-based model, although higher values of $D_{e_{max}}$ reduced the computational cost of simulations, as fewer increments were required to corrode samples. It should be noted that elements must still not be allowed to completely corrode within a single increment (e.g. $D_{e_{max}} < 0.99$).

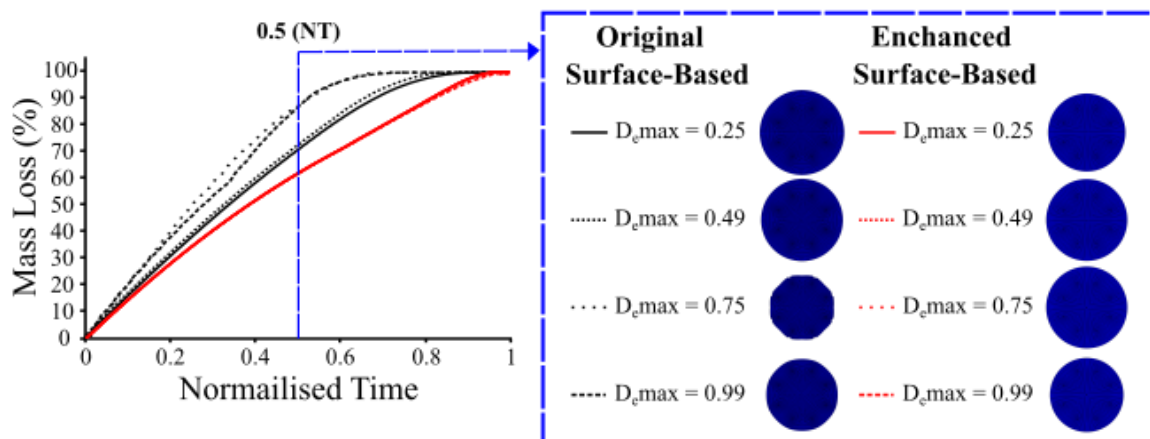


Figure 12 - Percentage mass loss for uniform degradation of original surface-based model and enhanced surface-based corrosion model at different allowable damage per increment ($D_{e_{max}}$). Degradation profiles were captured for each model was taken at a normalised time (NT) value of 0.5.

3.2 Model Predictions of Pitting Corrosion

3.2.1 Weibull Shape Parameter (γ)

The effect of the Weibull shape parameter (γ) on the formation of pitting corrosion was investigated through four separate parameter distribution values ($\gamma = 0.2, 0.4, 0.6$ and 0.8). The model geometry outlined in Figure 7 was implemented, alongside model parameters for model 7 described in Table 3. β -phase locations were highlighted by pitting parameter values λ_e and normalised pitting parameter values $\lambda_{e_{norm}}$ prior to degradation, shown in Figure 13A. Interestingly, the simulations using the enhanced surface-based corrosion algorithm produced varied multidirectional pits, as shown in Figure 13B. The pitting profile of the part constantly evolved as the part degraded, degrading in an unpredictable manner. As the shape parameter decreased from $\gamma = 0.8$ to $\gamma = 0.2$, the values of λ became more heterogeneous, thus leading to the formation of more localised elliptical pitting (see Figure 1D(ii)) and deep and narrow pitting (see Figure 1D(i)). As γ increased, pitting became more homogenous, resulting in wider and more shallow pitting (see Figure 1D(iii)). Additionally, the magnitude of pitting parameter values did not vary dramatically as the γ parameter was increased Figure 13A. Each simulation was created with an identical random seed, therefore similar pitting features were evident at different degrees of severity for each implemented Weibull shape parameter Figure 13B.

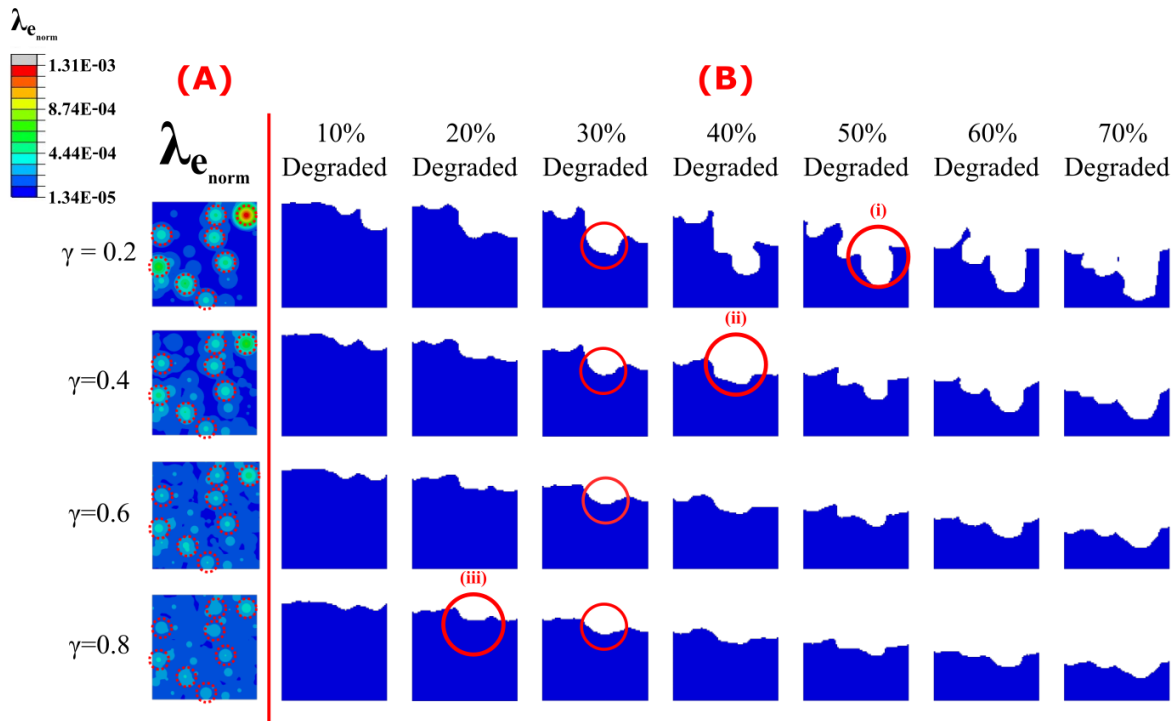


Figure 13 - (A) Contour plot of pitting parameter distribution ($\lambda_{e_{norm}}$) for $\gamma = 0.2, 0.4, 0.6$ and 0.8 . Dotted red circles represent the location of prominent pits. (B) Pitting corrosion profiles were captured at 10, 20, 30, 40, 50, 60 and 70 percent mass loss. Solid red circles represent similar pitting features

On the other hand, simulations degraded using the original surface-based model produced characteristic “cone-shaped” pitting that grew perpendicular to the corroding surface. Pitting profiles were completely controlled by the initial pitting parameter values assigned to the corroding surface, preventing the pitting profile from evolving as the part degraded. In this sense, the pitting profile at 10% degradation for each shape parameter was comparable to 70% degradation Figure 14B. Pitting parameter values varied dramatically as γ increased, with $\gamma = 0.2$ and $\gamma = 0.8$ resulting in a maximum value of $\lambda_e = 8,230$ and $\lambda_e = 8,801$ (see Figure 14A), which in turn greatly affect the corrosion rate. Clearly, the pits produced by this model are non-physical and bear little resemblance to the characteristic features described in Figure 1D(i-vii).

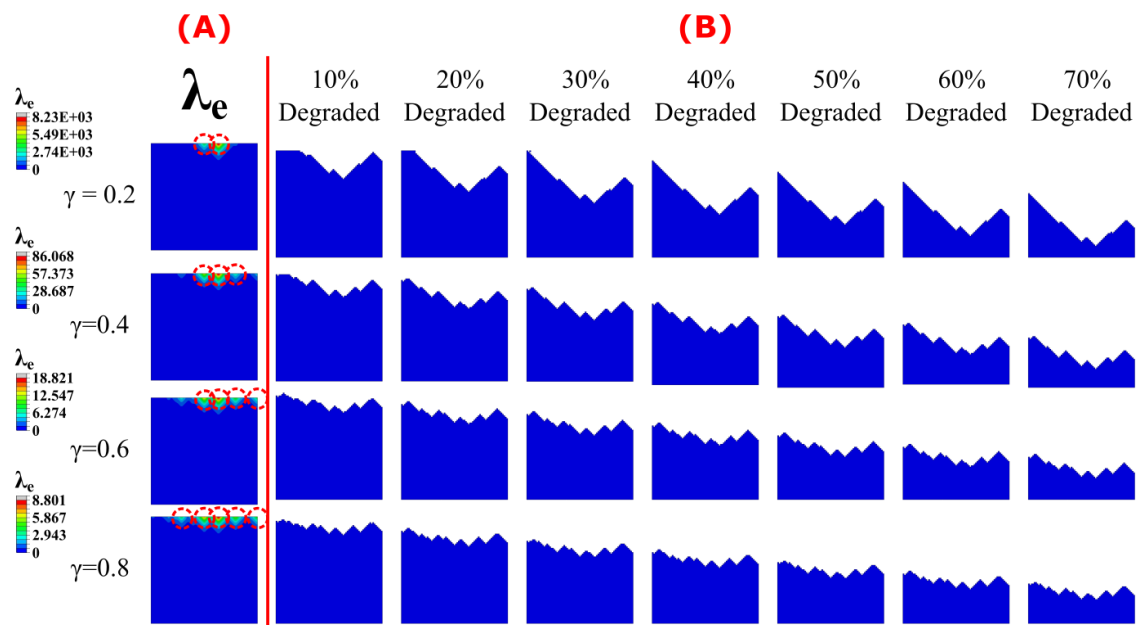


Figure 14 - (A) Contour plot of pitting parameter distribution (λ_e) for $\gamma = 0.2, 0.4, 0.6$ and 0.8 implementing the original surface-based algorithm (see Section 2.1). Dotted red circles represent the location of prominent pits. (B) Pitting corrosion profiles were captured at 10, 20, 30, 40, 50, 60 and 70 percent mass loss.

3.2.2 Random Seed

Each random seed implemented a pseudo-random number generation for the given Weibull parameters. The model geometry outlined in Figure 7 was implemented, alongside model parameters for model 7 described in Table 3. Altering the random seed generated a completely new set of random numbers λ_e , which altered pit locations, as shown in Figure 15A. A small amount of variance was observed in the number and severity of pits when altering random seed. Here, we show that the enhanced surface-based model can capture many of the different pit morphologies shown in Figure 1D, which are referenced with red circles within Figure 15B and include (i) deep & narrow, (ii) elliptical, (iii) wide & shallow, (iv) subsurface, (v) undercutting, (vi) horizontal and (vii) vertical. Elliptical (iii) and wide/shallow (ii) were the most common pit types to occur throughout all simulations. However more complex pitting

geometries: deep & narrow (i), subsurface (iv) and undercutting (v) were all generated at different degradation points Figure 15B.

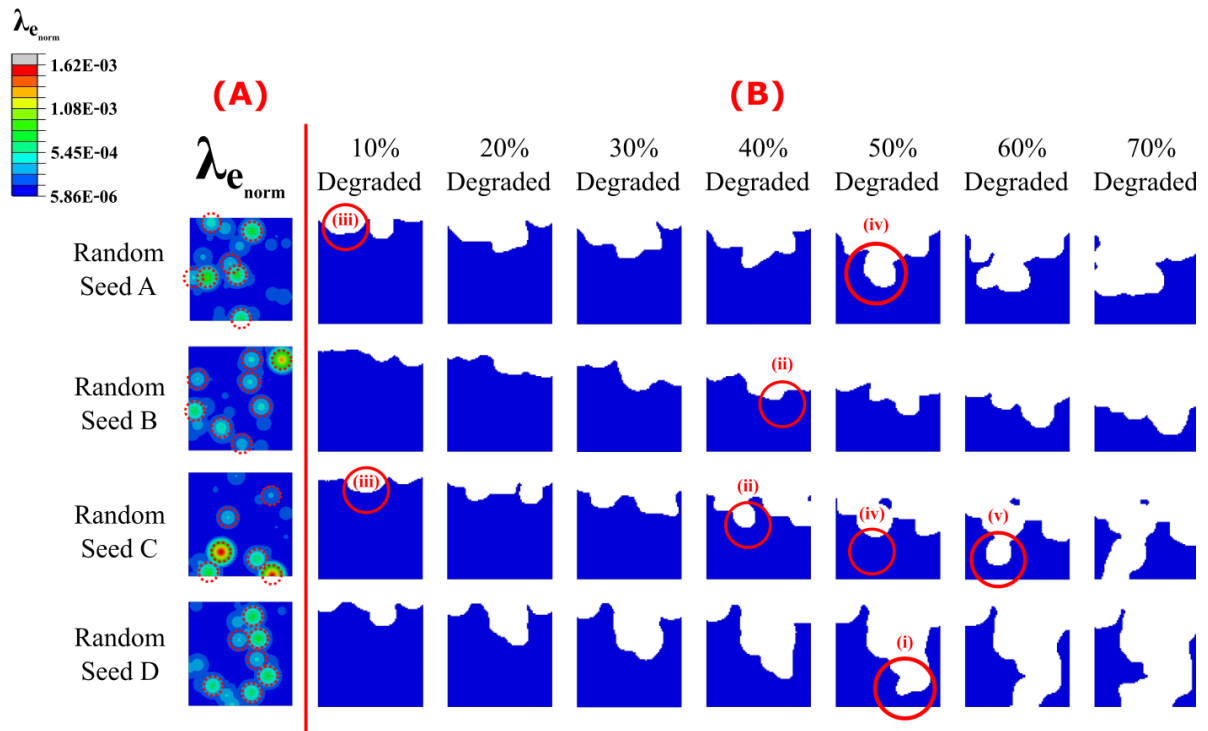


Figure 15 - (A) Contour plot of pitting parameter distribution ($\lambda_{e_{norm}}$) for four unique values of RS. Dotted red circles under $\lambda_{e_{norm}}$ heading represent the location of prominent pits. (B) Pitting corrosion profiles were captured at 10, 20, 30, 40, 50, 60 and 70 percent mass loss. Red circles represent the location different types of pitting outlined in Fig.18.

Simulations implementing the original surface-based algorithm once again had a large variance in the generated pitting parameter values λ_e . Seed A, B, C and D had maximum pitting values of $\lambda_e = 861.467, \lambda_e = 8,230.7, \lambda_e = 2,068.67$ & $\lambda_e = 3,392.16$ respectively for a constant Weibull shape parameter ($\gamma = 0.2$). Altering the random seed changed the pitting profile, however for each simulation the pitting profiles does not evolve as the part degraded. A clear dependency existed between the initial and final degraded states. Therefore, changing the RS only alters the initial state, see Figure 16A.

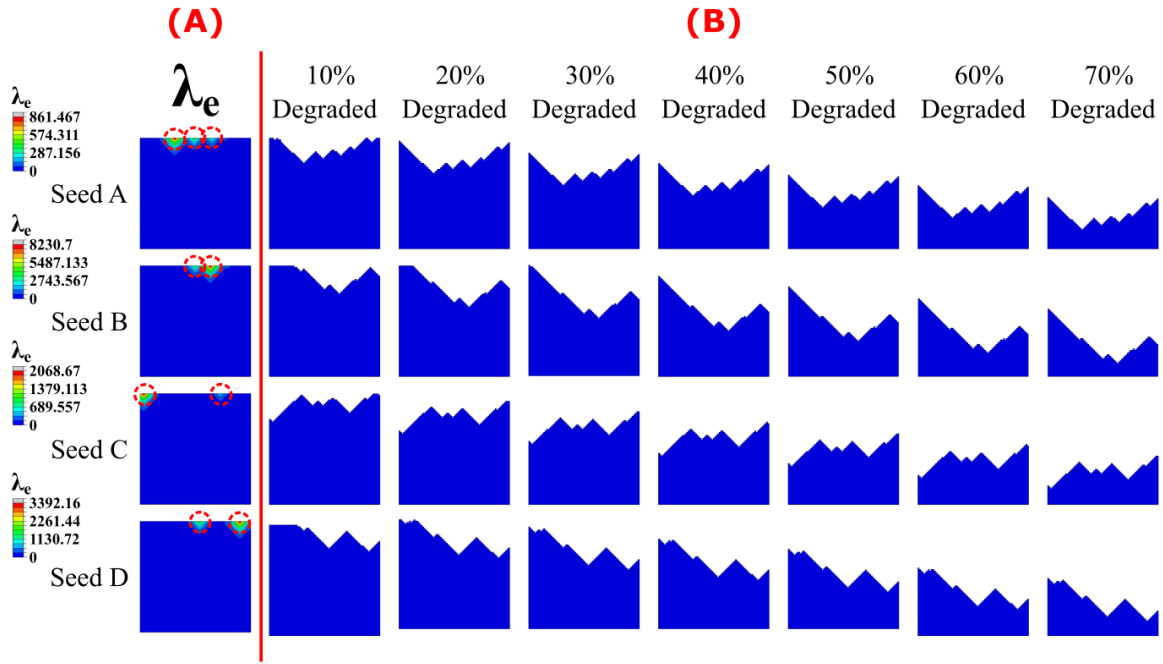


Figure 16 - Contour plot of pitting parameter distribution (λ_e) for four unique values of RS implementing the original surface-based algorithm (see Section 2.1). (B) Pitting corrosion profiles were captured at 10, 20, 30, 40, 50, 60 and 70 percent mass loss.

3.2.3 Characteristic Pit Radius (r_{pit})

The pit radius was controlled by altering the value of r_{pit} outlined in Equation(10). The model geometry outlined in Figure 7 was implemented, alongside model parameters for model 7 described in Table 3. The characteristic pit radius as described in Section 2.2.2 described how pitting parameter values were redistributed from pit nuclei. The assignment of r_{pit} determined the rate per unit distance pitting parameter values was lost from pit nuclei (see Figure 17A), thus determining the size of pitting features observed within corroded specimens (see Figure 17B). Constant Weibull shape parameters (γ) and random seed (RS) values were implemented for all simulations, therefore the differences in pitting profiles within Figure 17B were solely based on the assignment of r_{pit} . Reducing the value of r_{pit} resulted in the more nucleated assignment of pitting values ($\lambda_{e_{norm}}$) (see Figure 17A), thus resulting smaller and more irregular pitting features. Increasing r_{pit} allowed for a greater more uniform distribution of pitting values ($\lambda_{e_{norm}}$) (see Figure 17A), resulting in pitting features becoming more uniform (see Figure 17B).

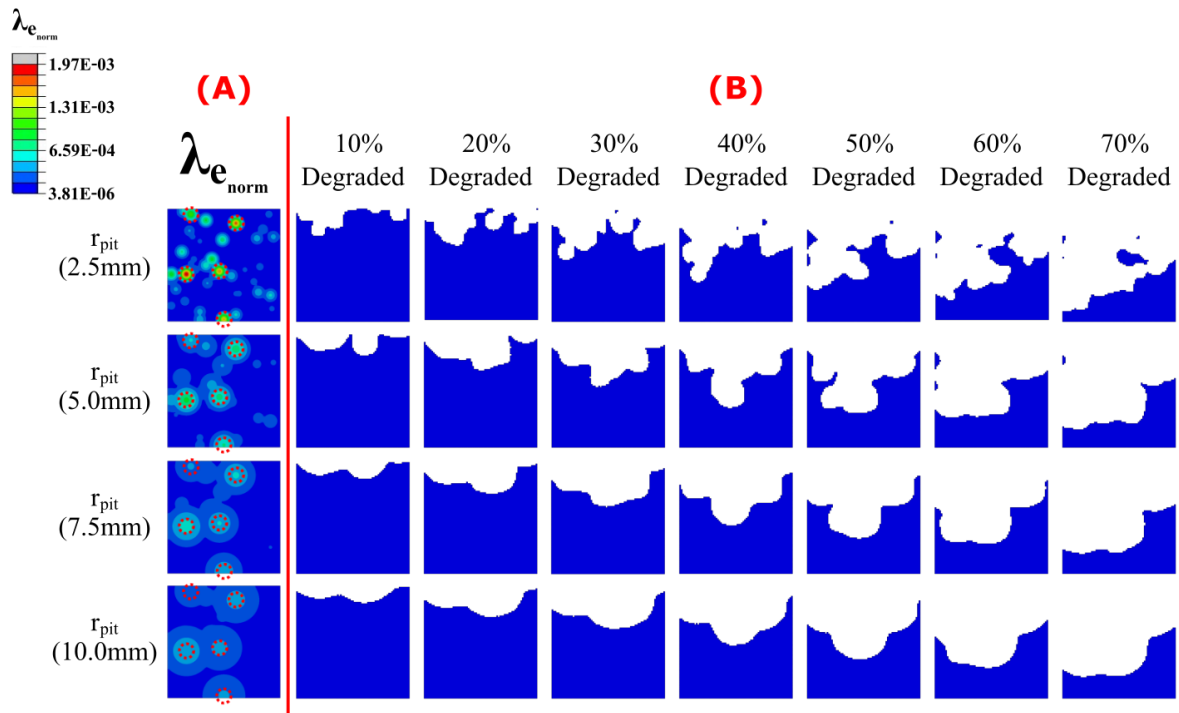


Figure 17 - (A) Contour plot of pitting parameter distribution ($\lambda_{e_{norm}}$) for different characteristic pit radius $r_{pit} = 2.5, 5, 7.5$ and 10mm . Dotted red circles represent the location of prominent pits. (B) Pitting corrosion profiles were captured at 10, 20, 30, 40, 50, 60 and 70 percent mass loss.

3.3 Three-dimensional implementation

The model geometry outlined within Figure 8 was implemented to on cylindrical dog-bone specimens. Model parameters $\gamma = 0.3$ and $r_{pit} = 0.8$ resulted were chosen to closely represents the experimental data at 14% and 53% mass loss, whereby probability distributions of pit depths are shown in Figure 18C & Figure 19C. During the initially stages of degradation the range of pit depths are tight and small as indivial pits form of the corroding surface (see Figure 18). As degradation develops the indivial pits merge to form larger pits, which results in a wider distribution function (see Figure 19).

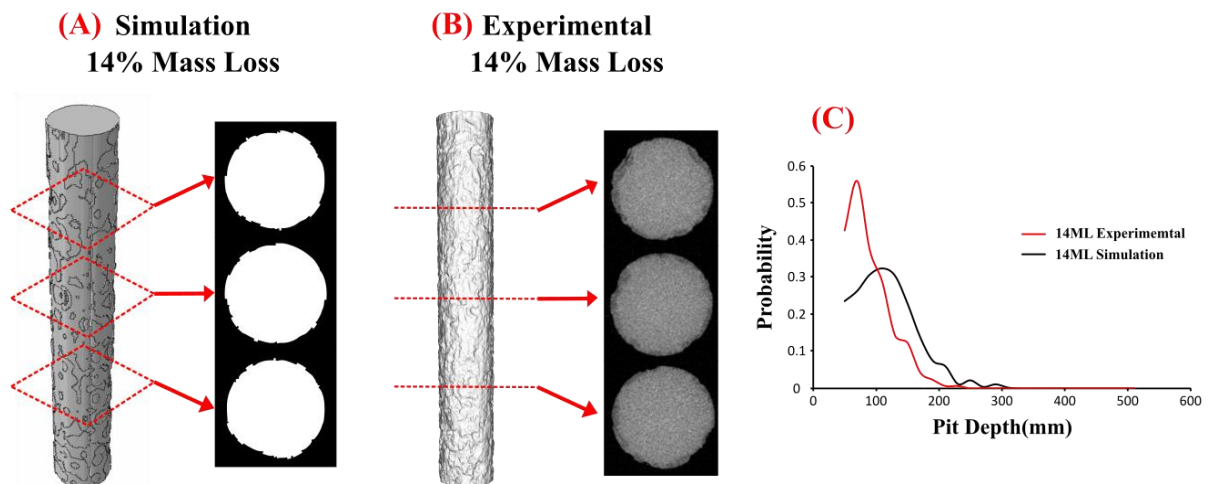


Figure 18 - Magnesium rod degraded to 14% mass loss with (A) computational framework and through (B) experimental methods. (C) Probability of pitting for both computational and experimental studies.

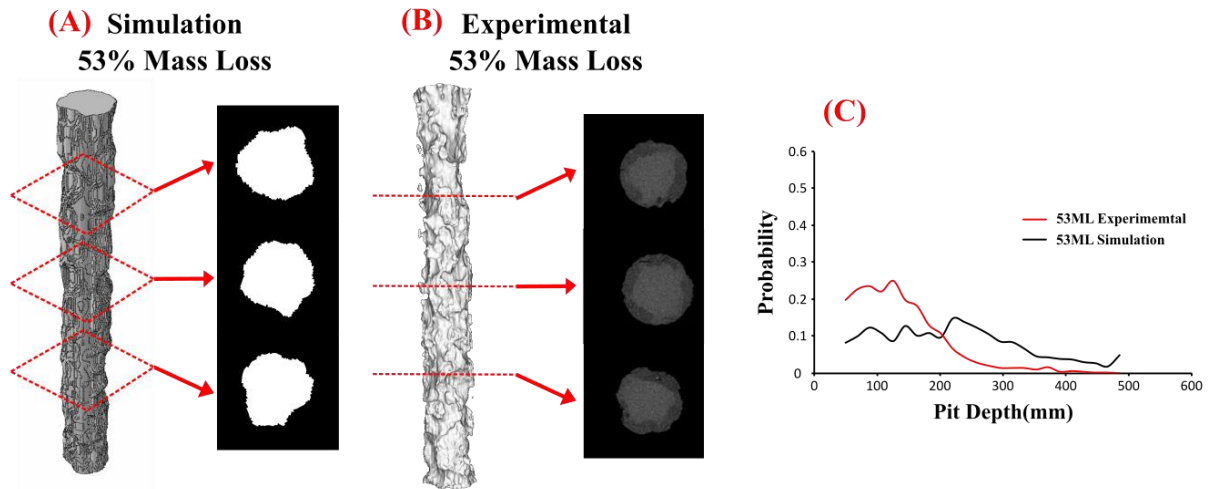


Figure 19 - Magnesium rod degraded to 53% mass loss implementation (A) simulation and (B) experimental methods. (C) Probability of pitting was compared for simulation and experimental results.

4. Discussion

This study developed an enhanced phenomenological model for surface-based localised corrosion of magnesium alloys. The modelling framework extended the approach by Grogan et al. [25] to more accurately capture spatial and temporal features of localised corrosion by considering the role β -phase components throughout the material volume. This enhanced surface-based corrosion model offers many advantages as it (i) captures multi-directional pitting, (ii) captures various pit morphologies, (iii) eliminates mesh sizing effects, (iv) reduces computational cost through custom time controls (v) offers control of pit sizing and (vi) produces corrosion rates that are independent of pitting parameter values. The model was fully implemented in three dimensions within the finite element framework and shows excellent potential to enable robust predictions of the long-term performance of magnesium-based implants undergoing corrosion.

The onset of localised surface-based corrosion in magnesium alloys presents distinct challenges in the design of medical implants as the load-bearing capacity of the implant is constantly changing during the device lifetime. While several phenomenological models [8, 29, 30, 36, 38] for surface-based corrosion have been developed, they suffer from several limitations, most notably that the entire corrosion process depends only on parameters prescribed on the initial exposed corrosion surface. Therefore, the evolution of localised corrosion in these models tends to be simplistic and models are unable to capture more intricate features such multi-directional or sub-surface pitting, phenomena that are well-described in experimental literature [15]. The primary contribution of this model is that we consider the role of impurities and inter-metallic phases in the entire material volume, which can potentially contribute to corrosion due to the evolving corroding surface. While the model is phenomenological, several of the models parameter do have a physical basis. For example, the Weibull shape parameter (γ) and random seed (RS) controlled the overall distribution of initial pitting parameter

values (λ_e) whose values represented the concentration and position of impurities and possible nucleation sites of β -phases within the material, which locally accelerate the corrosion rate. The characteristic pit radius (r_{pit}) controlled the range of influence pit nuclei imparted on the surrounding material, which ultimately controlled the size of observed pitting features within the degrading part. The corrosion rate parameter (k_u) dictated the overall corrosion rate encompassing physical, chemical, and biological factors, simplifying the complex interactions (and associated reaction rates) that occur between the corroding surface and surrounding environment.

In particular, the Weibull shape parameter (γ) controlled the variance of the distribution of random numbers (λ_e) across all elements in the model, which was a phenomenological representation of the physical distribution of the β phase throughout the magnesium alloy. The random seed parameter was used to initialize the pseudorandom number generation based on the prescribed Weibull distribution. While pseudorandom distributions are not truly random as they use deterministic, predictable algorithms, they are statistically random. For a given random seed, the location of prominent pit nuclei remained constant while the intensity of pit nuclei was altered through γ . This provided control over the intensity of pit nuclei throughout the material volume, which would alter the rate and direction of localised corrosion. While γ described the intensity of pit nuclei, r_{pit} described the range of influence pit nuclei had on the surrounding material, with based on their relative strength determining the corrosion characteristics of proximal elements, thus allowing for greater control of observed pitting features (see Figure 17B).

This approach allowed for new pitting features to be generated at any stage of corrosion and generation of unique pitting profiles and pit morphologies such as deep & narrow, elliptical, wide & shallow, subsurface, and undercutting, which is similar to those commonly observed from experiments [35]. (represented schematically in Figure 1D). Prediction of these complex features are in contrast to other phenomenological models that are only capable of producing a characteristic cone-shaped pits [25]. Until now, physically-based corrosion models would have been required to capture such processes, although these have been generally at the level of an individual pit [28]. However, physically-based models are not easily applicable to larger geometries due to the high computation cost associated with modelling electrochemical reactions [8]. Our enhanced surface-based model also included targeted optimisation of computational time, while ensuring model accuracy through a time control that controlled the maximum damage increment ($D_{e_{max}}$) that could occur within a single increment making it highly adaptable to larger structures. Greater control over pit morphology was also possible through the introduction of r_{pit} , which allowed for the redistribution of λ_e to be scaled with distance and determined the influence a single pit nucleus had within the model. Through the manipulation of r_{pit} and γ it may be possible to match a wide array of experimental corrosion profiles; (i) numerous severe small pits ($\gamma = \text{high}$, $r_{pit} = \text{low}$), (ii) numerous severe large pits ($\gamma = \text{high}$, $r_{pit} = \text{high}$), (iii) few weak

small pits ($\gamma = \text{low}$, $r_{pit} = \text{low}$) and (iv) few weak large pits ($\gamma = \text{low}$, $r_{pit} = \text{high}$). Through altering r_{pit} and γ the number, severity and size of pitting features can be approximately controlled for a given random seed.

Our enhanced surface-based corrosion model also offers several advantages in its numerical implementation as it eliminated the effects of mesh discretisation and model parameter sensitivity on the spatial and temporal progression of corrosion. These features are known to severely impact other surface-based corrosion models [8, 30, 36]. Model verification was carried out to ensure that the continuous process of corrosion was robustly captured within the discretized finite element framework. Within the enhanced surface-based corrosion model, the key parameters of corrosion rate (k_w, L_{active}) and corrosion shape (γ, r_{pit}) were independent of each other. Within the enhanced model, the implementation of L_{active} achieved uniform corrosion regardless of mesh structure by considering the precise geometry of elements. Previous papers commonly utilized a characteristic length parameter (L_e) to describe the element dimension, which only accurately described perfectly square/cubic elements and therefore resulted in inaccuracies in the corrosion rate of irregular element shapes (see Figure 9). The impact of mesh effects was highlighted through the implementation of irregular meshing within simple geometries under uniform corrosion, due to the predictability of the result. For uniform degradation, mesh density had no influence on corrosion rate for the enhanced surface-based model (see Figure 10A), unlike the original surface-based algorithm. For the latter, the redistribution of λ_e upon element removal was not scaled according to distance. Increasing element density increased the rate at which pitting parameter values were lost over a given distance. Therefore, altering the mesh density affected the size of pitting features created in the original surface-based algorithm. Within the enhanced surface-based algorithm, the redistribution of λ_e was scaled according to distance Equation (10), ensuring mesh density did not influence the size of pitting features generated (see Figure 10). Additionally, the enhanced surface-based model ensured that altering the mesh density and Weibull beta parameter (γ) did not affect the sum of pitting values within the degrading part, which meant that the overall corrosion rate remained constant, regardless of parameter selection. This is well demonstrated for the uniform corrosion case ($\lambda_e = 1$) when both the original and enhanced surface-based models are compared (see Figure 10A). Therefore, the sum of pitting parameter values within the volume-based algorithm was adjusted according to Equation (12), such that the sum of pitting parameter values within the part was set to equal the number of elements within the corroding part. This allowed for the convergence of the corrosion rate within the volume-based model upon increasing the mesh density (see Figure 10B) and minimised the effect the shape parameters (γ, r_{pit}) had on corrosion rate (see Figure 11). The small changes in corrosion rate observed within Figure 11 were primarily due to the relative strength and position of pit nuclei within the degrading part.

Within this study the framework of a magnesium corrosion model was created, however there are certain limitations to be acknowledged, and some scope for further development. The corrosion rate of magnesium was ultimately controlled through a static the rate parameter (k_u), numerous papers [29, 39, 40] implement a more realistic approach whereby degradation rate could be better captured using a non-linear rate function. Generally, these models consider corrosion as a diffusion-controlled process driven by the dissolution of magnesium. However, modelling different corrosion mechanisms accounting for all electrochemical and mechanical phenomena represents a difficult challenge, which hopefully this model can be further developed to achieve. Also, this model assumes that corrosion of magnesium is independent of the stress/strain state. However, there is evidence that corrosion of magnesium can be affected by the loading stage, with researchers proposing that corrosion can be captured through the addition of a strain-based criteria [41] As magnesium-based implants are commonly used in load bearing applications, the addition of strain-based corrosion could provide further enhancement to the model and valuable insight for device design.

5. Conclusion

In this study an enhanced surface-based corrosion model was developed to simulate localized pitting caused by galvanic corrosion in magnesium alloys. This enhanced surface-based corrosion model offers many advantages as it (i) captured multi-directional pitting, (ii) captured various pit morphologies, (iii) eliminated mesh sizing effects, (iv) reduced computational cost through custom time controls (v) offered control of pit sizing and (vi) produced corrosion rates that were independent of pitting parameter values. This model allowed a wide range of pitting profiles and pit morphologies to be captured, similar to those observed in the experimental literature. In addition, more complex features of corrosion including subsurface pitting and undercutting could even be captured through this novel approach. The model was fully implemented in three dimensions within the finite element framework and shows excellent potential to enable robust predictions of the long-term performance of magnesium-based implants undergoing corrosion (i.e. degradation in the human body).

6. Funding

Funding support was provided by the Irish Research Council (IRC) Government of Ireland Postgraduate Scholarship (GOIPG/2017/ 2021).

References

- [1] M. P. Staiger, A. M. Pietak, J. Huadmai, and G. Dias, "Magnesium and its alloys as orthopedic biomaterials: a review," (in eng), *Biomaterials*, vol. 27, no. 9, pp. 1728-34, Mar 2006, doi: 10.1016/j.biomaterials.2005.10.003.
- [2] J. J. Jacobs, "Metal Release in Patients Who Have Had
a Primary Total Hip Arthroplasty," *J Bone Joint Surg Am*, vol. 80-A, 1998.
- [3] J. J. Jacobs, J. L. Gilbert, and R. M. Urban, "Corrosion of metal orthopaedic implants," (in eng), *J Bone Joint Surg Am*, vol. 80, no. 2, pp. 268-82, Feb 1998, doi: 10.2106/00004623-199802000-00015.
- [4] C. Lhotka, T. Szekeres, I. Steffan, K. Zhuber, and K. Zweymüller, "Four year study of Co and chromium blood levels in patients managed with two different metal-on-metal total hip replacements," *Journal of orthopaedic research : official publication of the Orthopaedic Research Society*, vol. 21, pp. 189-95, 04/01 2003, doi: 10.1016/S0736-0266(02)00152-3.
- [5] M. Abdalla, A. Joplin, M. Elahinia, and H. Ibrahim, "Corrosion Modeling of Magnesium and Its Alloys for Biomedical Applications: Review," *Corrosion and Materials Degradation*, vol. 1, no. 2, pp. 219-248, 2020. [Online]. Available: <https://www.mdpi.com/2624-5558/1/2/11>.
- [6] K. B. Deshpande, "Numerical modeling of micro-galvanic corrosion," *Electrochimica Acta*, vol. 56, no. 4, pp. 1737-1745, 2011/01/15/ 2011, doi: <https://doi.org/10.1016/j.electacta.2010.09.044>.
- [7] F. Witte, "The history of biodegradable magnesium implants: A review," *Acta Biomaterialia*, vol. 6, no. 5, pp. 1680-1692, 2010/05/01/ 2010, doi: <https://doi.org/10.1016/j.actbio.2010.02.028>.
- [8] D. Gastaldi, V. Sassi, L. Petrini, M. Vedani, S. Trasatti, and F. Migliavacca, "Continuum damage model for bioresorbable magnesium alloy devices — Application to coronary stents," *Journal of the Mechanical Behavior of Biomedical Materials*, vol. 4, no. 3, pp. 352-365, 2011/04/01/ 2011, doi: <https://doi.org/10.1016/j.jmbbm.2010.11.003>.
- [9] L. Choudhary and R. K. Raman, "Magnesium alloys as body implants: fracture mechanism under dynamic and static loadings in a physiological environment," (in eng), *Acta Biomater*, vol. 8, no. 2, pp. 916-23, Feb 2012, doi: 10.1016/j.actbio.2011.10.031.
- [10] R. K. S. Raman and L. Choudhary, "Cracking of magnesium-based biodegradable implant alloys under the combined action of stress and corrosive body fluid: a review," *Emerging Materials Research*, vol. 2, no. 5, pp. 219-228, 2013, doi: 10.1680/emr.13.00033.
- [11] M. B. Kannan and R. K. Raman, "In vitro degradation and mechanical integrity of calcium-containing magnesium alloys in modified-simulated body fluid," (in eng), *Biomaterials*, vol. 29, no. 15, pp. 2306-14, May 2008, doi: 10.1016/j.biomaterials.2008.02.003.

- [12] M. Bobby Kannan, R. K. Singh Raman, F. Witte, C. Blawert, and W. Dietzel, "Influence of circumferential notch and fatigue crack on the mechanical integrity of biodegradable magnesium-based alloy in simulated body fluid," (in eng), *J Biomed Mater Res B Appl Biomater*, vol. 96, no. 2, pp. 303-9, Feb 2011, doi: 10.1002/jbm.b.31766.
- [13] M. Bobby Kannan and R. K. Singh Raman, "Evaluating the stress corrosion cracking susceptibility of Mg–Al–Zn alloy in modified-simulated body fluid for orthopaedic implant application," *Scripta Materialia*, vol. 59, no. 2, pp. 175-178, 2008/07/01/ 2008, doi: <https://doi.org/10.1016/j.scriptamat.2008.03.001>.
- [14] R.-c. Zeng *et al.*, "Review of studies on corrosion of magnesium alloys," *Transactions of Nonferrous Metals Society of China*, vol. 16, pp. s763-s771, 2006/06/01/ 2006, doi: [https://doi.org/10.1016/S1003-6326\(06\)60297-5](https://doi.org/10.1016/S1003-6326(06)60297-5).
- [15] G. L. Song and A. Atrens, "Corrosion Mechanisms of Magnesium Alloys," *Advanced Engineering Materials*, vol. 1, no. 1, pp. 11-33, 1999, doi: [https://doi.org/10.1002/\(SICI\)1527-2648\(199909\)1:1<11::AID-ADEM11>3.0.CO;2-N](https://doi.org/10.1002/(SICI)1527-2648(199909)1:1<11::AID-ADEM11>3.0.CO;2-N).
- [16] H. Henry, N. Xueyuan, and M. Yueyu, "Corrosion and Surface Treatment of Magnesium Alloys," in *Magnesium Alloys*, C. Frank Ed. Rijeka: IntechOpen, 2014.
- [17] W. E. Mercer and J. E. Hillis, "The Critical Contaminant Limits and Salt Water Corrosion Performance of Magnesium AE42 Alloy," presented at the International Congress & Exposition, feb, 1992. [Online]. Available: <https://doi.org/10.4271/920073>.
- [18] J. A. Richardson and G. C. Wood, "A study of the pitting corrosion of Al by scanning electron microscopy," *Corrosion Science*, vol. 10, no. 5, pp. 313-323, 1970/01/01/ 1970, doi: [https://doi.org/10.1016/S0010-938X\(70\)80023-3](https://doi.org/10.1016/S0010-938X(70)80023-3).
- [19] A. Aballe, M. Bethencourt, J. Botana, M. J. Cano, and M. Marcos-Bárcena, "Influence of the cathodic intermetallics distribution on the reproducibility of the electrochemical measurements on AA5083 alloy in NaCl solutions," *Corrosion Science - CORROS SCI*, vol. 45, pp. 161-180, 01/31 2003, doi: 10.1016/S0010-938X(02)00067-7.
- [20] G. Song, A. Atrens, D. S. John, X. Wu, and J. Nairn, "The anodic dissolution of magnesium in chloride and sulphate solutions," *Corrosion Science*, vol. 39, no. 10, pp. 1981-2004, 1997/10/01/ 1997, doi: [https://doi.org/10.1016/S0010-938X\(97\)00090-5](https://doi.org/10.1016/S0010-938X(97)00090-5).
- [21] H. Ibrahim, S. N. Esfahani, B. Poorganji, D. Dean, and M. Elahinia, "Resorbable bone fixation alloys, forming, and post-fabrication treatments," *Materials Science and Engineering: C*, vol. 70, pp. 870-888, 2017/01/01/ 2017, doi: <https://doi.org/10.1016/j.msec.2016.09.069>.
- [22] M. M. Gawlik, B. Wiese, V. Desharnais, T. Ebel, and R. Willumeit-Römer, "The Effect of Surface Treatments on the Degradation of Biomedical Mg Alloys-A Review Paper," (in eng), *Materials (Basel)*, vol. 11, no. 12, Dec 16 2018, doi: 10.3390/ma11122561.

- [23] F. Cosmi, N. Steimberg, and G. Mazzoleni, "A mesoscale study of the degradation of bone structural properties in modeled microgravity conditions," (in eng), *J Mech Behav Biomed Mater*, vol. 44, pp. 61-70, Apr 2015, doi: 10.1016/j.jmbbm.2015.01.002.
- [24] N. Shayesteh Moghaddam *et al.*, "Metals for bone implants: safety, design, and efficacy," *Biomanufacturing Reviews*, vol. 1, no. 1, p. 1, 2016/10/06 2016, doi: 10.1007/s40898-016-0001-2.
- [25] J. A. Grogan, B. J. O'Brien, S. B. Leen, and P. E. McHugh, "A corrosion model for bioabsorbable metallic stents," *Acta Biomaterialia*, vol. 7, no. 9, pp. 3523-3533, 2011/09/01/ 2011, doi: <https://doi.org/10.1016/j.actbio.2011.05.032>.
- [26] S. Scheiner and C. Hellmich, "Stable pitting corrosion of stainless steel as diffusion-controlled dissolution process with a sharp moving electrode boundary," *Corrosion Science*, vol. 49, no. 2, pp. 319-346, 2007/02/01/ 2007, doi: <https://doi.org/10.1016/j.corsci.2006.03.019>.
- [27] S. Scheiner and C. Hellmich, "Finite Volume model for diffusion- and activation-controlled pitting corrosion of stainless steel," *Computer Methods in Applied Mechanics and Engineering*, vol. 198, no. 37, pp. 2898-2910, 2009/08/01/ 2009, doi: <https://doi.org/10.1016/j.cma.2009.04.012>.
- [28] N. J. Laycock and S. P. White, "Computer Simulation of Single Pit Propagation in Stainless Steel under Potentiostatic Control," *Journal of The Electrochemical Society*, vol. 148, no. 7, p. B264, 2001, doi: 10.1149/1.1376119.
- [29] M.-M. Mohammad, A. Wahhaj, L. Muzi, G. Carlos, and L. Javier, "Simulation of corrosion and mechanical degradation of additively manufactured Mg scaffolds in simulated body fluid," *Journal of the Mechanical Behavior of Biomedical Materials*, vol. 126, p. 104881, 2022, doi: <https://doi.org/10.1016/j.jmbbm.2021.104881>.
- [30] J. A. Grogan, S. B. Leen, and P. E. McHugh, "A physical corrosion model for bioabsorbable metal stents," *Acta Biomaterialia*, vol. 10, no. 5, pp. 2313-2322, 2014/05/01/ 2014, doi: <https://doi.org/10.1016/j.actbio.2013.12.059>.
- [31] J. C. Walton, "Mathematical modeling of mass transport and chemical reaction in crevice and pitting corrosion," *Corrosion Science*, vol. 30, no. 8, pp. 915-928, 1990/01/01/ 1990, doi: [https://doi.org/10.1016/0010-938X\(90\)90013-U](https://doi.org/10.1016/0010-938X(90)90013-U).
- [32] S. M. Sharland, C. P. Jackson, and A. J. Diver, "A finite-element model of the propagation of corrosion crevices and pits," *Corrosion Science*, vol. 29, no. 9, pp. 1149-1166, 1989/01/01/ 1989, doi: [https://doi.org/10.1016/0010-938X\(89\)90051-6](https://doi.org/10.1016/0010-938X(89)90051-6).
- [33] K. van Gaalen, F. Gremse, F. Benn, P. E. McHugh, A. Kopp, and T. J. Vaughan, "Automated ex-situ detection of pitting corrosion and its effect on the mechanical integrity of rare earth magnesium alloy - WE43," *Bioactive Materials*, vol. 8, pp. 545-558, 2022/02/01/ 2022, doi: <https://doi.org/10.1016/j.bioactmat.2021.06.024>.

- [34] K. van Gaalen, C. Quinn, F. Benn, P. E. McHugh, A. Kopp, and T. J. Vaughan, "Linking the effect of localised pitting corrosion with mechanical integrity of a rare earth magnesium alloy for implant use," *Bioactive Materials*, vol. 21, pp. 32-43, 2023/03/01/ 2023, doi: <https://doi.org/10.1016/j.bioactmat.2022.08.004>.
- [35] "Different Types of Corrosion." https://www.corrosionclinic.com/types_of_corrosion/pitting_corrosion.htm (accessed).
- [36] A. Amerinatanzi, R. Mehrabi, H. Ibrahim, A. Dehghan, N. Shayesteh Moghaddam, and M. Elahinia, "Predicting the Biodegradation of Magnesium Alloy Implants: Modeling, Parameter Identification, and Validation," (in eng), *Bioengineering (Basel)*, vol. 5, no. 4, Nov 29 2018, doi: 10.3390/bioengineering5040105.
- [37] Y. Gao, L. Wang, X. Gu, Z. Chu, M. Guo, and Y. Fan, "A quantitative study on magnesium alloy stent biodegradation," (in eng), no. 1873-2380 (Electronic).
- [38] E. L. Boland, J. A. Grogan, and P. E. McHugh, "Computational modelling of magnesium stent mechanical performance in a remodelling artery: Effects of multiple remodelling stimuli," *International Journal for Numerical Methods in Biomedical Engineering*, vol. 35, no. 10, p. e3247, 2019, doi: <https://doi.org/10.1002/cnm.3247>.
- [39] G. Ann-Kathrin *et al.*, "A simulation model for the degradation of magnesium-based bone implants," *Journal of the Mechanical Behavior of Biomedical Materials*, vol. 101, p. 103411, 2020, doi: <https://doi.org/10.1016/j.jmbbm.2019.103411>.
- [40] S. Zhenquan *et al.*, "Predicting the degradation behavior of magnesium alloys with a diffusion-based theoretical model and in vitro corrosion testing," *Journal of Materials Science & Technology*, vol. 35, no. 7, pp. 1393-1402, 2019, doi: <https://doi.org/10.1016/j.jmst.2019.02.004>.
- [41] E. Galvin, C. Lally, B. Mac Donald, C. Cummins, D. O'Brien, and D. Mathews, *A strain-mediated corrosion model for bioabsorbable metallic stents*. 2015.